Journal of Solid State Chemistry 274 (2019) 270–279

Contents lists available at ScienceDirect

Journal of Solid State Chemistry

journal homepage: www.elsevier.com/locate/jssc

Environmental remediation properties of Bi_2WO_6 hierarchical nanostructure: A joint experimental and theoretical investigation

Marisa de Jesus Silva Chaves [a], Gênesis de Oliveira Lima [a], Marcelo de Assis [b], Cáritas de Jesus Silva Mendonça [a], Ivo Mateus Pinatti [b], Amanda Fernandes Gouveia [c], Ieda Lúcia Viana Rosa [b], Elson Longo [b], Marcio Aurélio Pinheiro Almeida [d,*], Teresa Cristina Rodrigues dos Santos Franco [e]

[a] Departamento de Química, Universidade Federal do Maranhão, Campus do Bacanga, 1966, CEP 65085-580, São Luís MA, Brazil
[b] CDMF, Universidade Federal de São Carlos, P.O. Box 676, CEP 13565-905, São Carlos SP, Brazil
[c] Departamento de Química, Universidade Estadual do Piauí, P.O. Box 381, CEP 64002-150, Teresina PI, Brazil
[d] Coordenação de Ciência e Tecnologia, Universidade Federal do Maranhão, Campus do Bacanga, 1966, CEP 65085-580, São Luís MA, Brazil
[e] Departamento de Tecnologia Química, Universidade Federal do Maranhão, Campus do Bacanga, 1966, CEP 65085-580, São Luís MA, Brazil

ARTICLE INFO

Keywords:
Bismuth tungstate
Photocatalysis
Photoluminescence

ABSTRACT

In this work, different structures of Bi_2WO_6 (BWO) were synthesized using a template-assisted microwave process. The BWO samples were characterized using various methods such as X-ray Diffraction (XRD), Scanning Electron Microscopy (SEM), Diffuse Reflectance Spectroscopy (DRS), and Raman Spectroscopy. The results show that the templates were able to promote changes in morphology and electronic properties. The photocatalytic experiment showed higher photocatalytic activity in RhB dye under UV light irradiation for the BWO sample, as compared with other samples. This behavior was attributed to better crystallinity and lower e^-/h^+ pair recombination rates supported by XRD and photoluminescence experiments.

1. Introduction

Currently, the rise in world population is associated with an increase in pollutants released into the environmental [1], which are responsible for several diseases for people living in the vicinity, promoted by contamination vectors such as fish, fruit, and water. One factor of great concern is wastewater released into rivers and lakes, because this is responsible for the contamination of foods, which are ultimately consumed by humans. Water contaminants can be classified into pesticides [2,3], herbicides [2], and dye organics [4].

Since the discovery of the photocatalytic properties of TiO_2 in organic and inorganic molecules by Fushima et al. [5], many oxide-based compounds have been observed to have similar properties [6]. These compounds have shown to be capable of assisting remediation in contaminated environments, either by mineralization/degradation or the adsorption process. Both degradation and adsorption are processes that are related to the physical-chemical properties of the surface of materials. Consideration of the surface chemistry is very important to the development of new materials with active surfaces, which can be used in several photocatalysis processes and can assist the adsorption of hazardous substances in the environment. The inorganic semiconductors developed in the last few years have been very effective in this realm; depending on the method used for the synthesis of the nanomaterials, their surface proprieties can be completely changed.

Various studies have demonstrated the potential of semiconductors to remove environmental contaminants via adsorption [7]. Liu et al. obtained α-Fe_2O_3 using poly-vinylpyrrolidone (PVP)-modified rGO nanocomposite [8]. These compounds exhibited excellent adsorption performance for Rhodamine B (RhB), which was attributed to the charge on the surface created during the synthesis process. Otero et al. [9] synthesized Mg-Al hydrotalcite by calcination at 500 °C for 3 h, which was able to remove the pesticides Nicosulfuron and Mecoprop-P. Several studies [4,10] have considered advanced oxidative processes (AOP). Specifically, metal tungstates were found to be excellent materials for the remediation of wastewater [11,12].

Bismuth tungstate (Bi_2WO_6 – BWO) has an orthorhombic phase with the $P2_1ab$ and $B2cb$ structure [13,14], and has exhibited great versatility in catalytic applications, such as obtaining hydrogen [15], selective

* Corresponding author.
E-mail address: almeida.pinheiroa@gmail.com (M.A.P. Almeida).

https://doi.org/10.1016/j.jssc.2019.03.031
Received 24 August 2018; Received in revised form 27 February 2019; Accepted 17 March 2019
Available online 23 March 2019
0022-4596/

oxidation of glycerol [16], and degradation of dyes and antibiotic pollutants [17]. Bi_2WO_6 has two phase transitions and can undergo structural change, which is important for catalytic properties. Yan-jun et al. [18] synthesized the nanostructure of Bi_2WO_6 using a hydrothermal method that uses PVP and cetyl trimethyl ammonium bromide (CTAB) as surfactants. This synthesis yielded morphology completely different, in order from rod-like and particle-like (PVP) and plate-like for the CTAB morphology. The photocatalyst caused methyl orange to degrade by 67.14% and 20.00% under simulated sunlight for compounds obtained by PVP and CTAB, respectively. This change was attributed to the crystallization caused by these surfactants.

To improve the photocatalytic activity of Bi_2WO_6, Ying et al. [19] obtained a series of Sr-doped Bi_2WO_6 compounds that present nest-like structures using a hydrothermal method. These compounds exhibited catalytic properties in the degradation of RhB under visible-light irradiation ($\lambda > 420$ nm). These materials showed different degradation profiles based on the doping variation for Sr^{2+} ions, resulting in different surface defect content. Therefore, in this paper, we aim to study the importance of the microwave-assisted method and the use of the surfactants PVP, CTAB, and SDS (sodium dodecyl sulfate) in the hierarchical process in the development of new structured materials with different catalytic characteristics. To gain further insight, we performed density functional theory (DFT) calculations using the CRYSTAL14 program [20] to complement the experimental results, understand the physical phenomena occurring in the structure, determine the electronic and optical properties involved in the orthorhombic Bi_2WO_6 structure, and improve the photocatalytic mechanism.

2. Experimental

2.1. Material synthesis

In a typical synthesis, in a beaker with 100 mL of surfactant solution (PVP, CTAB, and SDS) in Milli-Q water, were added 0.3332 g (2.0 mmol) of sodium tungstate dihydrate ($Na_2WO_42H_2O$ Sigma-Aldrich, 99%) and 0.9899 g of bismuth nitrate pentahydrate ($Bi(NO_3)_35H_2O$ Sigma-Aldrich, 98%). The mixture was stirred for 10 min, then put into an autoclave and processed in a microwave system for 50 min at 180 °C. The powder was separated, washed separately with Milli-Q water and ethanol, and stored in a muffle furnace for 8 h at 60 °C to remove humidity. The samples obtained were called BWO, BWO-PVP, BWO-CTAB, and BWO-SDS, for those obtained without surfactant, with PVP, with CTAB, and with SDS, respectively.

2.2. Material characterization

The samples were characterized by X-ray diffraction (XRD) using a D/Max-2500PC diffractometer (Rigaku, Japan) with Cu-Kα radiation (1.5406 Å) at 40 kV and 150 mA, with 2θ range 5–100°, confirming the structures obtained previously [21]. The Raman spectra were obtained by Raman microscopy/spectroscopy (Bruker-RFS 100, Germany). The Raman spectra were obtained using a 1064 nm line with a Nd:YAG laser, with the maximum output power at 50 mW and using the range from 100 to 1100 cm^{-1}. The diffuse reflectance spectroscopy (DRS) measurements were performed using a Varian spectrophotometer, model Cary 5G. These analyses were carried out in the powder mode (bulk) using a $BaSO_4$-like reference standard. The scanning electron microscopy (SEM) images were obtained using a field-emission scanning electron microscope (FEG-SEM), the Carl Zeiss Supra 35-VP (Germany), operated at 10 kV. The photoluminescence (PL) measurements were performed using a Monospec 27 monochromator (Thermal Jarrel Ash, USA) coupled to an R446 photomultiplier, as described in previous works [22]. The monochromator used a krypton ion laser at 350 nm as the excitation source. All PL measurements were carried out at room temperature.

2.3. Photocatalytic experiments

In a photocatalytic reactor was added to 100 mL of solution (1.0×10^{-5} mol/L of Rh 6G dye) and 100 mg of the sample (BWO, BWO-PVP, BWO-CTAB, or BWO-SDS). The mixture was lifted by stirring for 30 min in the dark to achieve a desorption/adsorption equilibrium. Next, the sample was irradiated (350–420 nm) under stirring for 180 min. During this process, diverse aliquots were collected, centrifuged, and the concentration of the solutions containing Rh 6G was analyzed in a UV–Vis spectrometer (Shimadzu, UV–Vis 18000). All experiments were carried out at 25 °C and their kinetics were assumed to be pseudo-first order. For analysis of the possible radicals in the catalytic medium, we added a small amount of scavenger agent (sodium azide, superoxide, or isopropanol alcohol) to the solutions.

2.4. Computational method

Simulations of the Bi_2WO_6 crystal were performed using a periodic approximation, implemented in CRYSTAL14 computer code [23,24]. The computational method is based on DFT, in conjunction with the B3LYP hybrid functional [25,26]. The diagonalization of the Fock matrix was performed at adequate *k*-point grids in the reciprocal space. Thresholds controlling the accuracy of the calculation of the Coulomb and exchange integrals were set to 10-8 (ITOL1 to ITOL4) and 10–14 (ITOL5); the percentage of the Fock/Kohn–Sham matrix mixing was set to 40. Atomic centers for Bi and W atoms were described using the pseudopotential basis sets of Weihrich and Cora, respectively, and O atoms were described using 6-31d1, where all bases were provided by the CRYSTAL basis set library [20]. The Raman modes and their corresponding frequencies were calculated using numerical second derivatives of total energies as implemented in the CRYSTAL14 package. The electronic band structure and the density of states (DOS) were calculated using Porperties14 in CRYSTAL14; the structures were constructed along the high-symmetry directions of the corresponding irreducible Brillouin zone.

3. Results and discussion

3.1. Structural analysis

Fig. 1(a–d) shows the XRD patterns for the BWO (a), BWO-PVP (b), BWO-CTAB (c), and BWO-SDS (d) samples. All compounds presented

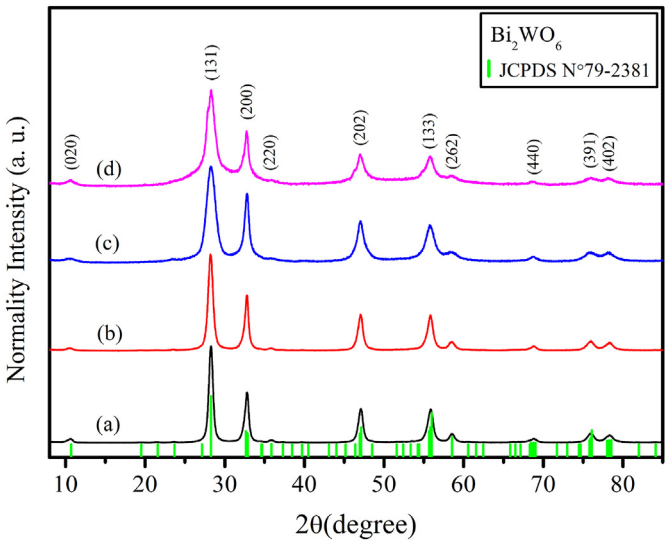

Fig. 1. XRD patterns of BWO crystals. (a) BWO, (b) BWO-CTAB, (c) BWO-PVP, and (d) BWO-SDS.

orthorhombic phase (JCPDS 79–2381) with the space group $P2_1ab$ [27]. The BWO orthorhombic phase has two possible space groups: symmetry *$P2_1ab$ and B2cb* that can be interchanged. The usual BWO structure has $P2_1ab$ orthorhombic phase according to the JCPDS 79–2381. On the other hand, induction to the *B2cb* metastable structure may happen in certain conditions of synthesis. However, all the samples synthesized presented the usual $P2_1ab$ structure mainly because of the microwave synthesis. Moreover, Fig. 1 clearly shows that there are no additional peaks, which indicates that the structure has a single phase. Another feature that can be seen in Fig. 1(b–d) is the enlargement of the peaks of the XRD patterns in the BWO-PVP, BWO-CTAB, and BWO-SDS samples when compared to the BWO sample, which can be correlated to the reduction of the crystallite sizes that will be further proven by the SEM images.

The Rietveld refinement method was employed to determine differences in the structural arrangements of the BWO samples prepared with and without the surfactants. In these analyses, the refined parameters of interest were the scale factor, background, shift lattice constants, profile half-width parameters (*u*, *v*, *w*), isotropic thermal parameters, lattice parameters, strain anisotropy factor, preferred orientation, and atomic functional positions. The background was corrected using a Chebyschev polynomial function of the first kind. The peak profile function was modeled using a convolution of the Thompson-Cox-Hastings pseudo-Voigt (pV-TCH) function [28] using the asymmetry function described by Finger et al. [29], which accounts for the asymmetry due to axial divergence. To account for the anisotropy in the half-width of the reflections, the model by Stephens [30] was used.

Rietveld refinement plots for the observed pattern versus the calculated pattern for all samples are shown in Fig. 2(a–d). The measured diffraction patterns matched very well to the JCPDS card N° 79–2381. The difference between XRD pattern profiles for experimentally observed and theoretically calculated data was small, at near zero in the intensity scale, as illustrated by the line ($Y_{Obs} - Y_{Calc}$). Details about the quality of the structural refinement, experimental lattice parameters, and calculated unit cell volumes are listed in Table 1, which shows small deviations of statistical parameters (R_{Bragg}, R_{wp}, and Gof). This behavior suggests that the refinement results are quite reliable and accurate. Structural refinement data confirm that all the samples crystallized in an orthorhombic structure with a symmetry space group termed Hermann-Mauguin ($P2_1ab$).

We observed a slight increase in the statistical parameters of quality values and an increase in the full width at half maximum (FWHM) of the (131) plane, when the BWO sample without surfactant was compared to the BWO-CTAB, BWO-PVP, and BWO-SDS samples. The sizes and types of carbon chains of the template are the main reasons for the differences observed. The longer the organic carbon chain and the greater the prevalence of cyclic chains, the more difficult will be the interaction between Bi and W polyhedrons. As a consequence, the phase is not in proper form and the amorphous part of these structures causes strain and stress in the orthorhombic framework. These small variations may also be related to the peculiarity of each sample. These templates have different effects on the experimental variables (temperature, time processing, heating rate, etc.) that likely modify the organization of the $[WO_6]$ and $[Bi_2O_2]$ layers within the crystal lattice. Additionally, these variables cause the formation of structural defects (oxygen vacancies, distortion of the bonds, stresses, and strains on the crystalline lattice) in the materials.

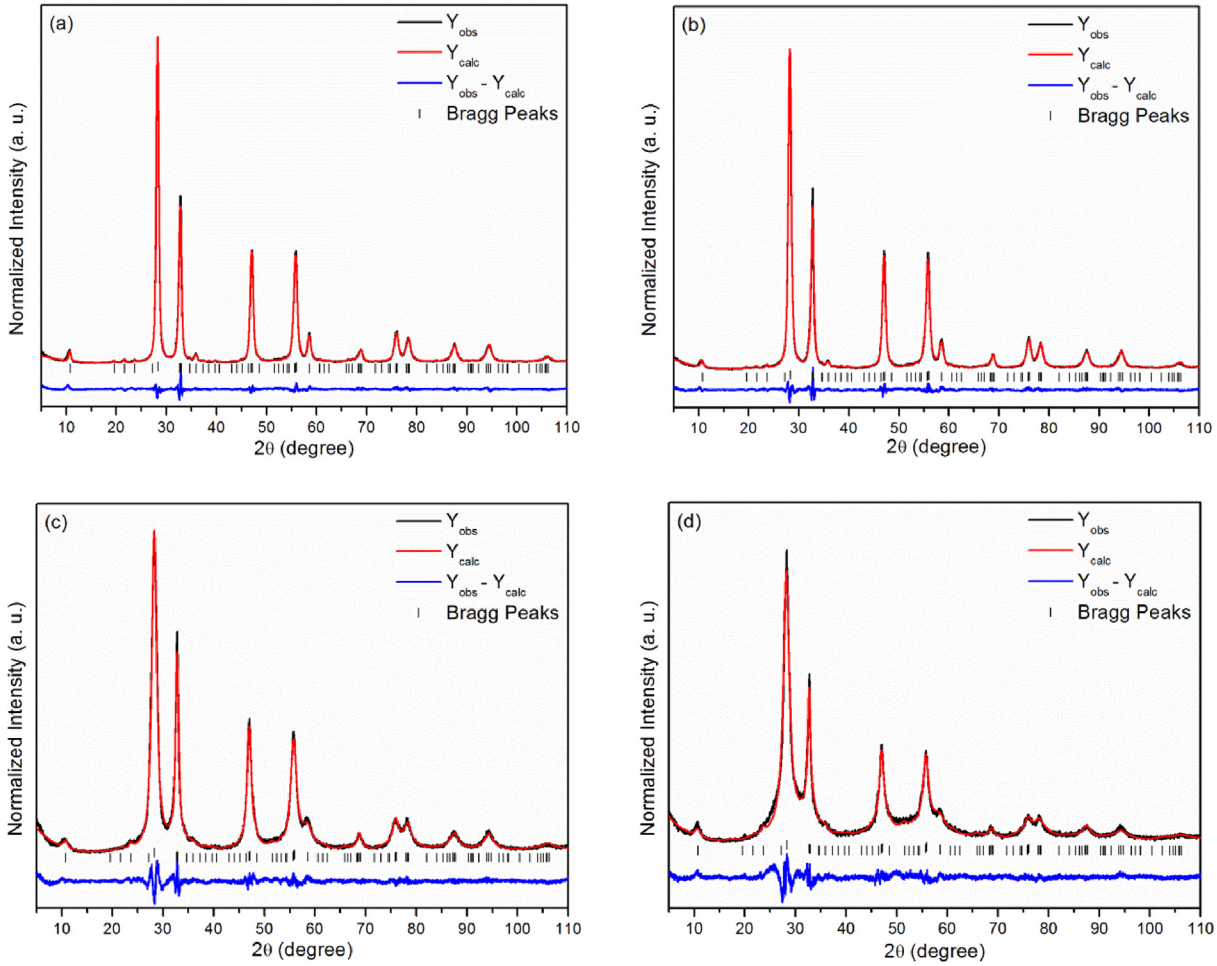

Fig. 2. Rietveld refinement plot of bismuth tungstate prepared whit different solvents. (a) BWO, (b) BWO-CTAB, (c) BWO-PVP, and (d) BWO-SDS.

Table 1
Lattice parameters, unit cell volume, and statistical parameters of quality obtained by Rietveld refinement for Bi_2WO_6 under different solvents.

Refined formula	Lattice parameters (Å)			Cell volume (Å^3)	R_{Bragg} (%)	R_{wp} (%)	Gof	FMWH (°)
	a	*b*	*c*					
BWO	5.447	5.451	16.415	487.431	1.01	7.62	1.73	1.19
BWO-CTAB	5.449	5.450	16.432	488.009	1.10	7.25	1.65	1.27
BWO-PVP	5.460	5.463	16.364	488.224	1.54	7.61	1.67	2.34
BWO-SDS	5.457	5.458	16.375	487.732	2.64	8.21	1.82	2.24
JCPDS Nº 79-2381	5.456	5.436	16.430	487.284	–	–	–	–

These defects result in similarly low crystallinity of the samples prepared with the templates when compared to the BWO [31].

A representation of the unit cell of an orthorhombic BWO-PVP microcrystal is presented in Fig. 3. This unit cell was modeled using the Visualization for Electronic and Structural Analysis (VESTA) program [32], version 3 for Windows®, and was modeled using lattice parameters and atomic positions obtained from the Rietveld refinement data shown in Table 1. Fig. 3 shows the existence of distorted polyhedrons with octahedral configuration for both Bi and W sites, which are coordinated to six O atoms. BWO with the orthorhombic structure belongs to the Aurivillius family [33], comprises alternating $(Bi_2O_2)_n^{2n+}$ layers and perovskite-like $(\mathbf{WO_4})_n^{2n-}$.layers. These polyhedrons are distorted in the crystal lattice owing to the difference in bond angles, which results in different order-disorder levels and/or distortions in the crystal lattice. In addition, the presence of different surfactants can also influence these distortions, which are confirmed by XRD and Rietveld refinement analyses.

A Raman spectral image of the BWO sample is shown in Fig. 4. The $P2_1ab$ structure of Bi_2WO_6, which is orthorhombic and belongs to the Aurivillius family [34], is related to 105 optical modes in an irreducible representation according to the group theory; $\Gamma = 26A_1 + 27A_2 + 26B_1 + 26B_2$ [35]. These irreducible transformations, and modes A_1, B_1, and B_2, are active in the Raman and IR images, whereas only A_2 modes are Raman-active. The active modes in the Raman image can be grouped as stretching vibrational $(2A_1 + 2A_2 + 2B_1 + 2B_2)$ to WO_6 octahedral and bending vibrational $(4A_1 + 4A_2 + 4B_1 + 4B_2)$ to WO_6 octahedral in the high-energy spectra. In the region of low energy, we have bending vibrations of the $(Bi_2O_2)^{2+}$ layer $(3A_1 + 3A_2 + 3B_1 + 3B_2)$, translational motion of the Bi^{3+} ions represented by $2A_1 + 2A_2 + B_1 + B_2$, and vibration involving the translational motion of Bi^{3+} and W^{6+} ions [36]. Thus, in the region of high energy, three modes are seen, at 825, 796, and 718 cm^{-1}, which may be attributed to the symmetric and asymmetric stretching vibrations of the WO_6 octahedral. In the range of low energy, we see highlights at 307, 283, and 152 cm^{-1}, which are attributed to bending modes of the WO_6 octahedral and $(Bi_2O_2)^{2+}$ layer. However, there are also modes of weak intensity in this range, which may be assigned to vibrations

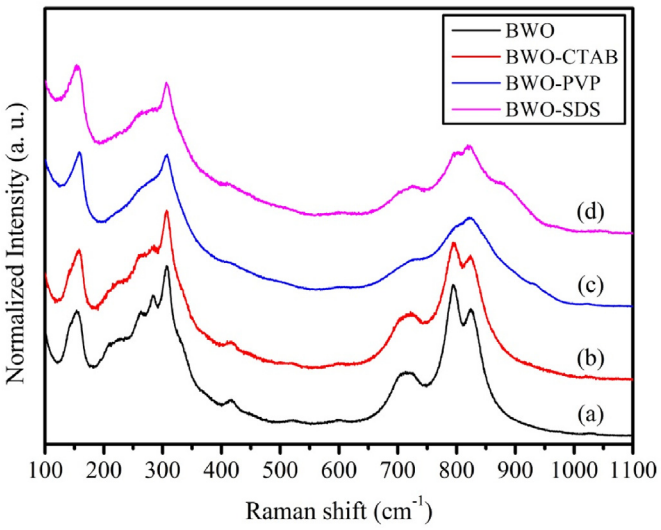

Fig. 4. Raman spectra of the as-synthesized samples. (a) BWO, (b) BWO-CTAB, (c) BWO-PVP, and (d) BWO-SDS.

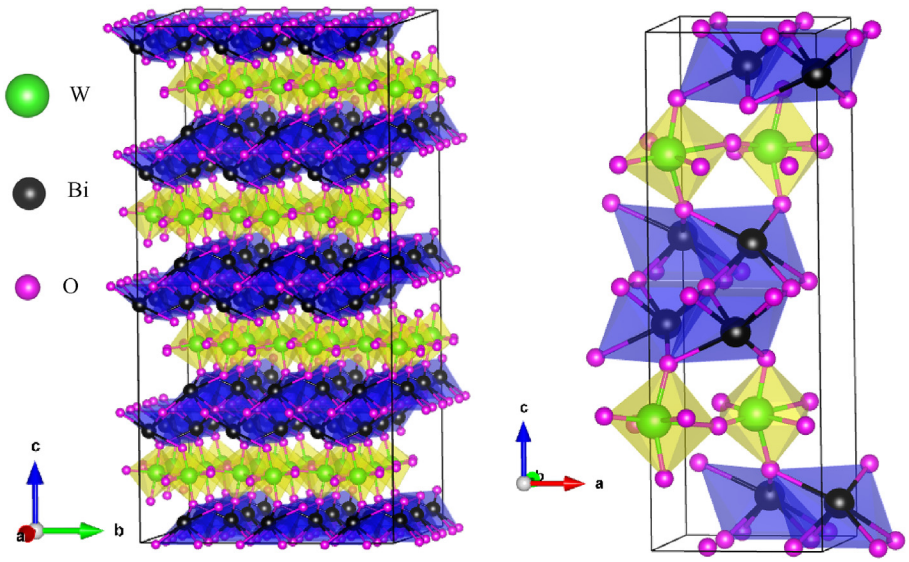

Fig. 3. Structure model of supercell 3 × 3 × 2 of Bi_2WO_6. (a) Bi_2WO_6 structure as alternating WO_6 and $Bi_2O_2^{2+}$ layers. (b) Coordination spheres of the tungsten and bismuth atoms in BWO.

involving the translational motion of Bi^{3+} and W^{6+} ions [36]. Also, it is interesting to notice that in Fig. 4(b–d) the enlargement of all the Raman peaks of the samples prepared in the presence of different templates were observed, which might indicate the presence of oxygen vacancy defects [37], as well as the reduction of the of crystallite sizes, as was also seen by Li et al. [38].

3.2. Morphological analysis

Fig. 5 shows SEM images of the BWO samples. These samples clearly show a high diversity of morphology. For BWO, the present morphology is not well-defined (leaf-like); the particles are able to agglomerate to create larger morphologies (see Fig. 5(a and b)). The morphology of BWO-PVP is shown in Fig. 4(c and d). In this SEM image, we see arose-like morphology, with a median size of 1.5 μm. The morphologies of BWO-CTAB and BWO-SDS, which are similar, but with different size, are shown in Fig. 6. In the SEM image, we observe that BWO-CTAB has smaller features than BWO-SDS. Both samples have no defined morphology, and few particles agglomerate to build more complex morphologies. Here, we see that the SEM images agree with the XRD patterns and Raman spectra described above, because they both display an increase in width, as compared with BWO, which suggests a reduction in the size of the crystallite. The use of CTAB, SDS, and PVP, directly influence the structural organization, to form different morphologies. The template CTAB, which is a positively charged organic molecule, seemed to have high stereo hindrance, causing the formation of nano-particles. Whereas for PVP, which is organic polymer neutral, we obtain the typical morphology, indicating that neutral molecules are better for this purpose. For SDS, we did not observe a change in the morphology, which suggests insufficient interaction during nucleation.

3.3. Optical properties

The band gap energy (E_g) is estimated based on the energy difference between the energy at the top of the valence band (VB) and bottom of the conduction band (CB). The theoretical calculation reveals an indirect band gap transitions for the BWO with the $P2_1ab$ space group. In this way, for the BWO semiconductor, the band gap value was estimated from the absorption spectra using the equation $\alpha h\nu = A(h\nu - E_g)^n$, where α, $h\nu$, A, n, and E_g are the absorption coefficient, light frequency, proportionality constant, transition type (where $n = 2$ is the indirect band gap), and band gap, respectively. Additionally, here we can consider α to be proportional to $F(r)$, the Kubelka-Munk function [39]. The band gap energy, E_g, can be calculated from the energy intercept of the plot of ($F(R)$ x $h\nu^2$ versus $h\nu$).

Fig. 7 shows the diffuse reflectance spectra of BWO samples, which were used to estimate the band gap values. For the obtained compound, BWO-CTAB had a band gap value $E_g = 3.40$ eV which was slightly higher than that of BWO ($E_g = 3.20$ eV). In contrast, the BWO-PVP and BWO-SDS samples exhibited different band gap energies, with low band gap values of 3.26 eV and 3.16 eV, respectively. Therefore, it is possible to affirm that the kind of surfactant has a huge influence on the electronic properties of the BWO. During structural organization on the microwave, the process of dissolution and re-crystallization possibility the high organization of the system resulting an increase of the band gap value or, can also, come out in a local disorder with a decrease in the band gap value, that are responsible by new levels between VB and CB, depending the surfactant used.

The electronic levels that form the electronic band structure of the BWO were analyzed using theoretical calculations. The optimized BWO structure presented an indirect band gap with a value of 4.22 eV between the S (VB) and X (CB) k-points in the Brillouin zone (see Fig. 8(a)). The high band gap value demonstrates that the theoretical structure of Bi_2WO_6 presents a greater structural order in the medium, short, and long ranges when compared to the experimental structure of BWO. This experimental value suggests that there are intermediate energy levels between VB and CB that were created based on the presence of impurities and/or surfactants.

To determine the atomic and orbital composition of the VB and CB that compose the electronic band structure which is associated with the

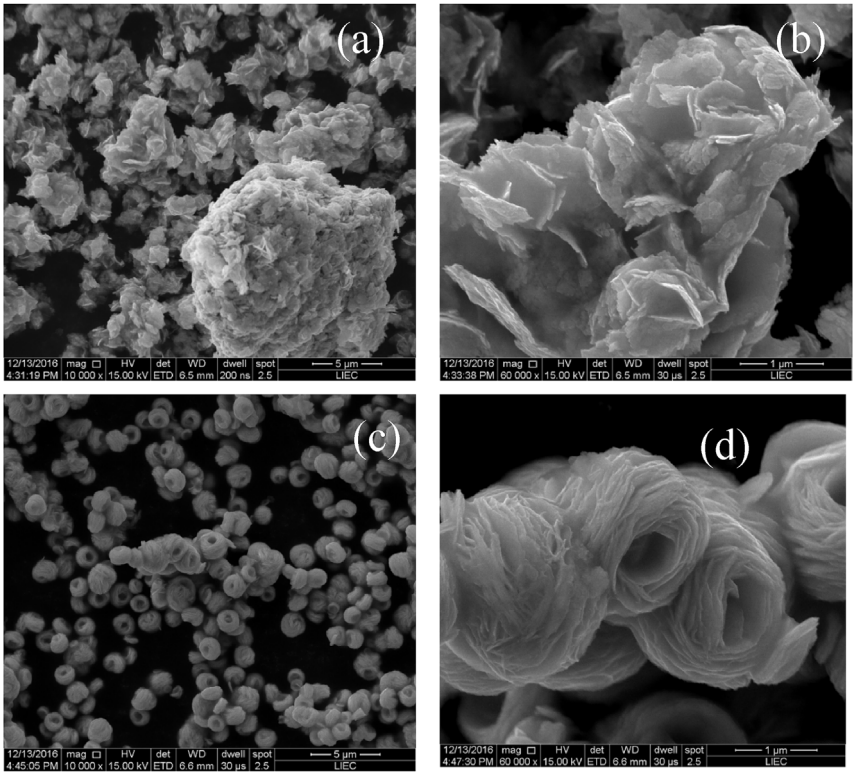

Fig. 5. Selected FEG-SEM micrographs for BWO samples. (a) BWO, (b) BWO with high magnification, (c) BWO-PVP, and (d) BWO-PVP with high magnification.

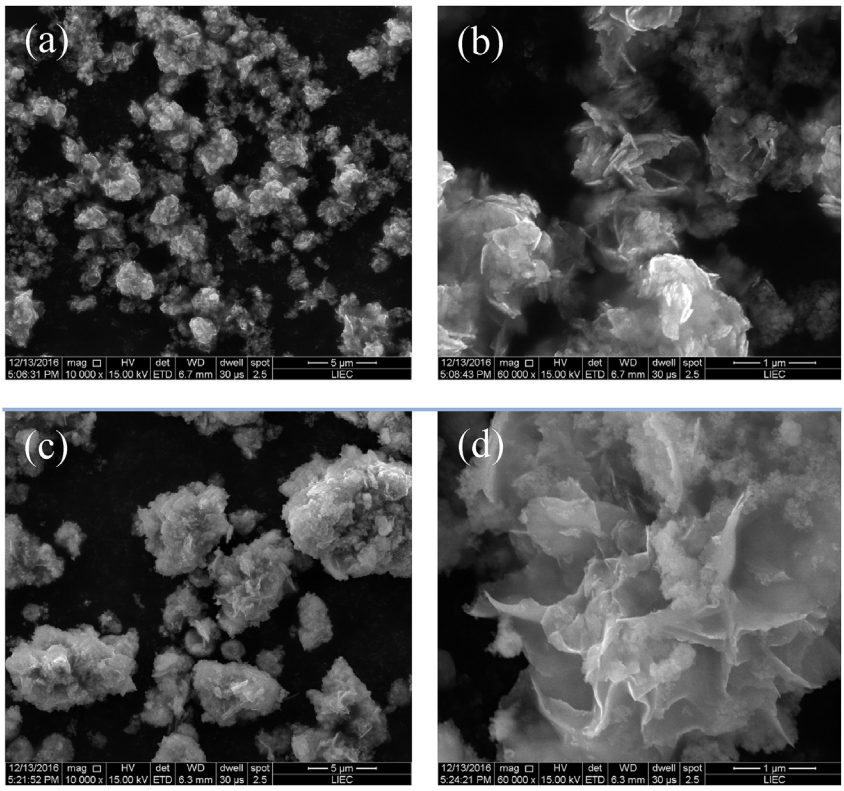

Fig. 6. Selected FEG-SEM micrographs for BWO samples. (a) BWO-CTAB, (b) BWO-CTAB with high magnification, (c) BWO-SDS, and (d) BWO-SDS with high magnification.

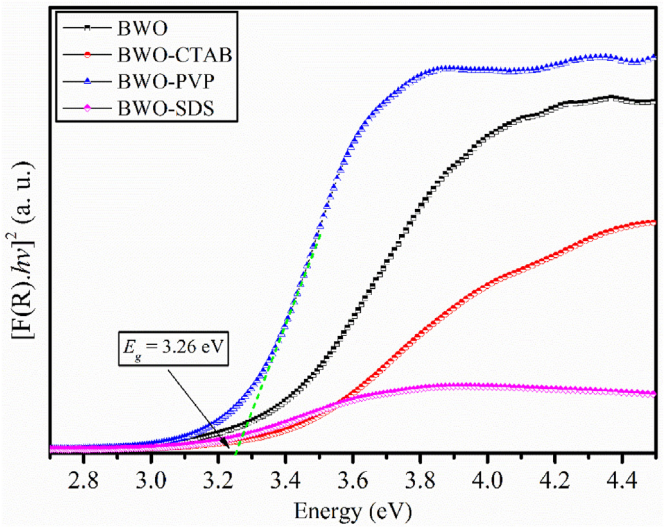

Fig. 7. UV–vis diffuse reflectance spectra of the BWO samples.

band gap region, it is necessary to study the density of states (DOS). Analyzing the DOS illustrated in Fig. 8(b), we observe that the VB is mainly composed of O and Bi atoms, whereas all atoms from the CB show the major contribution of W atoms. In the orbital analysis, we observe that the VB is mainly composed of O 2*p* and Bi 6*s* orbitals, whereas the W 5*d* orbitals have major contributions at the bottom of the CB, which is consistent with the literature [40,41]. The orbitals at the top of the VB are Bi 6*s* and O $2p_z$ orbitals; at the bottom of the CB the orbitals are Bi $6p_x$, W 5*d*, and O 3*s*.

In the PL emission spectra of BWO samples, the emission peaks are associated with electronic transfer between the $^1T_2$ state and holes in the $^1A_1$ state attributed to the $[WO_6]$ clusters [35]. The components at lower wavelengths are related to the regular crystal lattice, for which the emitting level contains Bi and W contributions. The components at higher wavelengths are ascribed to the defect centers associated with oxygen [41].

The PL emission spectrum of the BWO sample displays different profiles as it is showed in Fig. 9. The PL emission spectra of BWO and BWO-CTAB samples present a similar pattern, where both spectrum show broad bands centered at around 444 nm. In a different way, the PL emission spectra of BWO-PVP sample presented a strong emission band at around 496 nm (cyan region), while the PL emission spectrum of the BWO-SDS sample exhibit a weak emission band at around 444 nm (blue zone) and a shoulder with almost the same intensity at around 581 nm (yellow zone). Here we can see that the templates have strongly acted in the structural organization creating new localized states within the band gap, responsible by creating of deep, middle and shallow defects, it observed in Urbach tail, Fig. 7.

We also can see at Fig. 9 that the sample BWO-PVP has a much larger PL emission band than the other samples studied. Considering that the BWO sample has 100% emission because there are no changes from the addition of surfactants, we see that comparing BWO and the BWO-CTAB spectra there was a PL emission reduction of 39%. The BWO-SDS sample has an increase in PL emission of 59%, while the BWO-PVP sample presented a dramatic increase of 867%. To understand this behavior, the deconvolution of the PL spectra (Fig. 10) of the samples were obtained using the Voigt Area G/L function that resulted in three peaks centred at around 444 nm (blue), 496 nm (cyan), and 581 nm (yellow).

As shown in Fig. 9, the BWO and BWO-CTAB samples have very similar emission profiles, having a contribution of defects very similar: deep (581 nm), middle (495 nm) and shallow (444 nm). Thus, the CTAB template was not able to change the intensity of the PL emission drastically when compared with BWO sample, which suggests the same defect type, thus showing similar band gap values. When we analyzed the PL emission of the BWO-PVP sample (which is the most intense in the PL), it

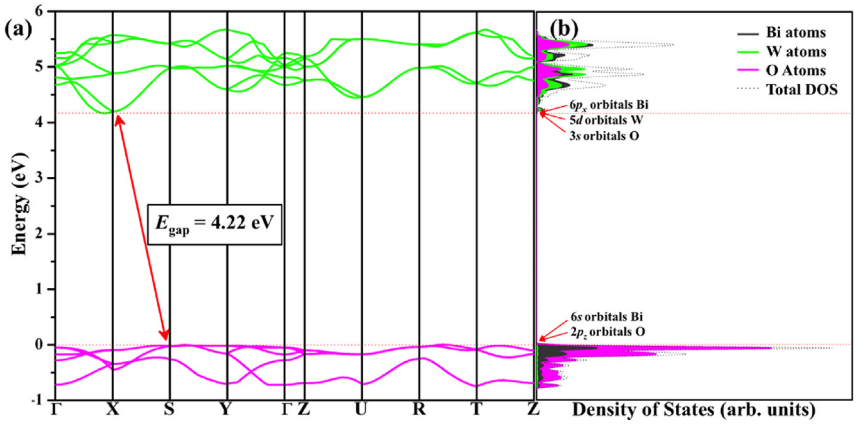

Fig. 8. (a) Electronic band structure and (b) density of states for Bi_2WO_6.

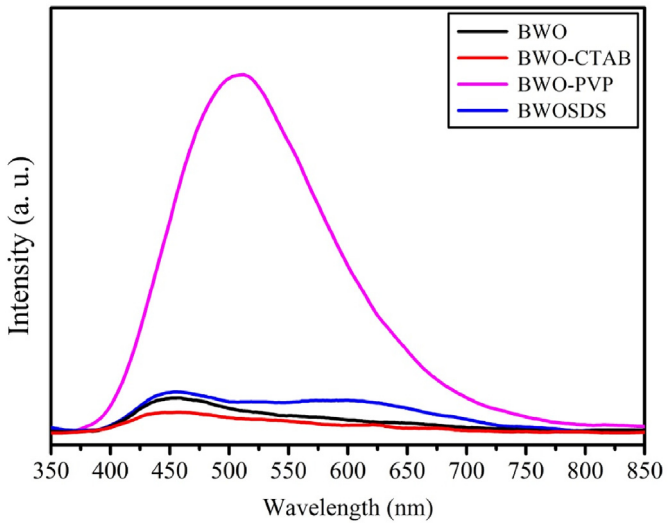

Fig. 9. Photoluminescence emission spectra of BWO, BWO-CTAB, BWO-PVP, and BWO-SDS.

was observed the loss of the band emission located at 444 nm. This lower wavelength band is linked with more energetic transitions between the valence band (VB) and the conduction band (CB) of the material, being directly connected to systematic structural defects within the sample. Therefore, using the PVP template, an increase in the lowest energy defects (medium and deep), which are directly associated with the formation of oxygen vacancies, which can promote the electron-hole recombination process, increasing the PL emission intensity [35]. When we notice the result for the BWO-SDS sample, it was observed the suppression of the shallow and medium defects, but in a much milder way than BWO-PVP. Thus, the high PL emission intensity for BWO-PVP sample can be attributed to the more contribution of the deep defects, when compared to the PL emission at 581 nm. These results are shown to be directly connected with the Raman and UV–Vis measurements, indicating a significant agreement between the techniques used.

3.4. Photocatalytic properties

Fig. 11(a) shows the absorption spectra of the degradation of dye with the use of the photocatalysts. During the degradation, a shift to high-energy range is exhibited, which can be ascribed to the partial degradation of methyl groups in the dye structural. This degradation leaves the dye deficient molecule in electronic density, justifying thus the shift of UV–vis absorption spectra to the wavelength of high-energy.

At 80 min, approximately 99% had degraded. This degradation is better evidenced by the decay curve kinetic in Fig. 11(b). This curve illustrates that, at 80 min, the photocatalysts BWO, BWO-CTAB, BWO-PVP, and BWO-SDS (slightly higher) achieved degradation ratios of 99, 89, 28, and 30%, respectively; the results are better illustrated in the degradation kinetics in Fig. 12(a).

Here, the different photocatalytic activity is associated with the different templates used in the reactional medium. For all compounds, the nanostructure dimensions are the same, but their electronic structures are completely different. Observing these structures and their respective band gap values, we hoped to show that the BWO-SDS sample presents better photocatalytic activity, and BWO-CTAB presents poor catalytic activity; however, this was not observed. BWO, as previously shown, presented better degradation than other compounds. This phenomenon might be directly related to the low combination rate of electron/hole (e'/h$^{\bullet}$) pairs, an assumption that is supported by the PL data in Fig. 8. As illustrated in Fig. 8, the compounds BWO-PVP and BWO- SDS have greater PL intensity, as compared with other samples, and highlight BWO-PVP, indicating a higher recombination rate of e'/h$^{\bullet}$ charge pairs. The compounds BWO and BWO-CTAB presented low-intensity PL, thus resulting in a reduction in the recombination rate of charges.

For a better understanding of the possible oxidant agents in the reactional medium, experiments using oxidative species scavengers (HO^-, $^1O_2$, O^{2-}) were used, as illustrated in Fig. 12(b). This Fig. shows that when benzoquinone was used as a scavenger in the reactional medium, a drastic reduction in the degradation of RhB was observed, as compared with isopropanol and sodium azide, with degradation values of 88.0 and 70.6%, respectively. Therefore, regarding the photodegradation mechanism, we suggest that for a dye irradiated by UV–Vis, electrons of the VB move to the CB. In the next step, the electrons of the dye CB are transferred to catalyst-forming clusters that are distorted ($[WO_6]_d^x/[BiO_6]_d^x$) or ordered ($[WO_6]_o^x$)/($[BiO_6]_o^x$). Thus, the ordered clusters with high electronic density, $[WO_6]_o^{'}(e_{CB}^-)/[BiO_6]_o^{'}(e_{CB}^-)$, can react with oxygen absorbed on the surface photocatalyst to form the superoxide radical, which is responsible for degradation of the RhB, as illustrated in equations (1)–(11) below.

$$Dye + UV-vis \rightarrow Dye(e'_{CB} + h^{\bullet}_{VB}) \quad (1)$$

$$Ads.dye(e'_{CB} + h^{\bullet}_{VB}) + [WO_6]_o^x \rightarrow [WO_6]'_o(e'_{CB}) + dye(h^{\bullet}_{VB}) \quad (2)$$

$$Ads.dye(e'_{CB} + h^{\bullet}_{VB}) + [BiO_6]_o^x \rightarrow [BiO_6]'_o(e'_{CB}) + dye(h^{\bullet}_{VB}) \quad (3)$$

$$[WO_6]_o^x + [WO_6]_d^x \rightarrow [WO_6]'_o(e'_{CB}) + [WO_6]^{\bullet}_d(h^{\bullet}_{VB}) \quad (4)$$

$$[BiO_6]_o^x + [BiO_6]_d^x \rightarrow [BiO_6]'_o(e'_{CB}) + [BiO_6]^{\bullet}_d(h^{\bullet}_{VB}) \quad (5)$$

$$[WO_6]^{\bullet}_d(h^{\bullet}_{VB}) + H_2O \rightarrow [WO_6]_d^x + OH^* + H^{\bullet} \quad (6)$$

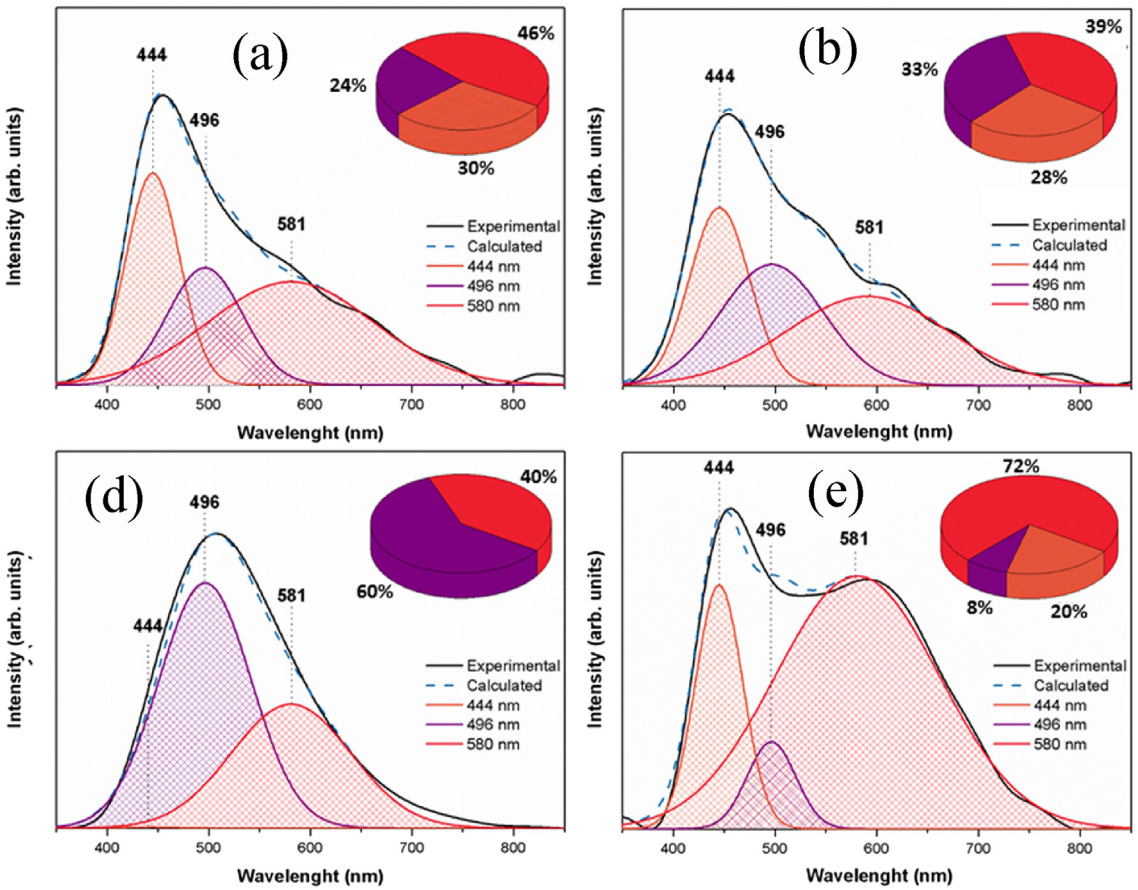

Fig. 10. Deconvolution of photoluminescence emission spectra of (a) BWO, (b) BWO-CTAB, (c) BWO-PVP, and (d) BWO-SDS.

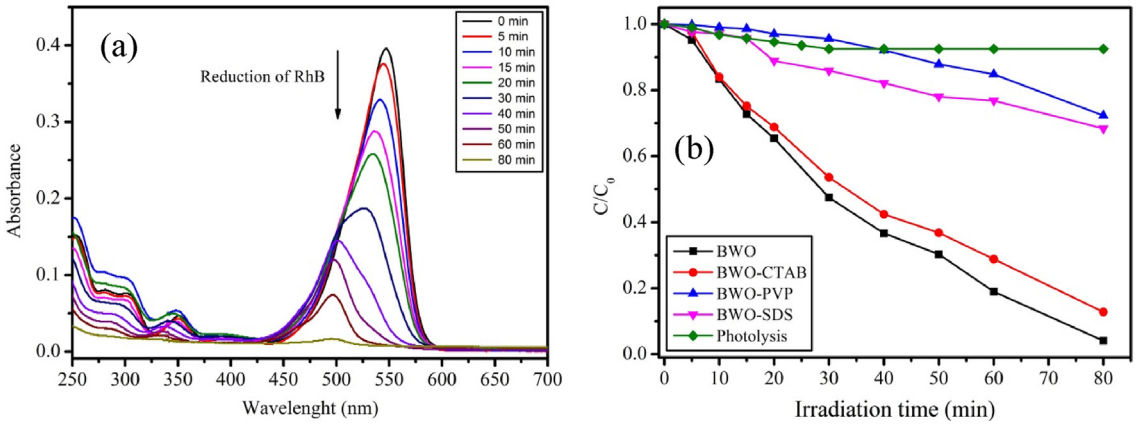

Fig. 11. Effect of different scavengers on the degradation of Rh 6G in the presence of a photocatalyst. (a) Degradation kinetics of Rh 6G using scavengers. (b) Decay curve of Rh 6G degradation using scavengers.

$$[BiO_6]_d^{\bullet}(h_{VB}^{\bullet}) + H_2O \rightarrow [BiO_6]_d^{x} + OH^{*} + H^{\bullet} \quad (7)$$

$$[WO_6]_o^{'}(e_{CB}^{'}) + O_2(or\ 2O) \rightarrow [WO_6]_o^{x} + O_2^{'} \quad (8)$$

$$[BiO_6]_o^{'}(e_{CB}^{'}) + O_2(or\ 2O) \rightarrow [BiO_6]_o^{x} + O_2^{'} \quad (9)$$

$$H^{\bullet} + O_2^{'} \rightarrow O_2H^{*} \quad (10)$$

$$OH^{*} + O_2H^{*} + dye \rightarrow degradated\ product \quad (11)$$

When the photocatalyst is irradiated, electrons from VB are excited to CB resulting separating of electron/hole (e'/h•) charge. These electrons at CB may be toward to activity surface, which can react with oxygen adsorbed on the surface of photocatalyst and form oxidative agents (radical superoxide), while the hole ate VB react with the water to split into a proton and hydroxyl radical. The reactive species, OH* (hydroxyl radical) and O_2H^* (perhydroxyl radical), formed by the interaction of the H_2O and O_2 with the hole and electron, respectively, on the top of the surface are responsible for photodegradation. Therefore, control of morphology in the synthesis of nanostructured material is of great importance to obtain activity surfaces.

In the synthesis using templates, we expected a structural change

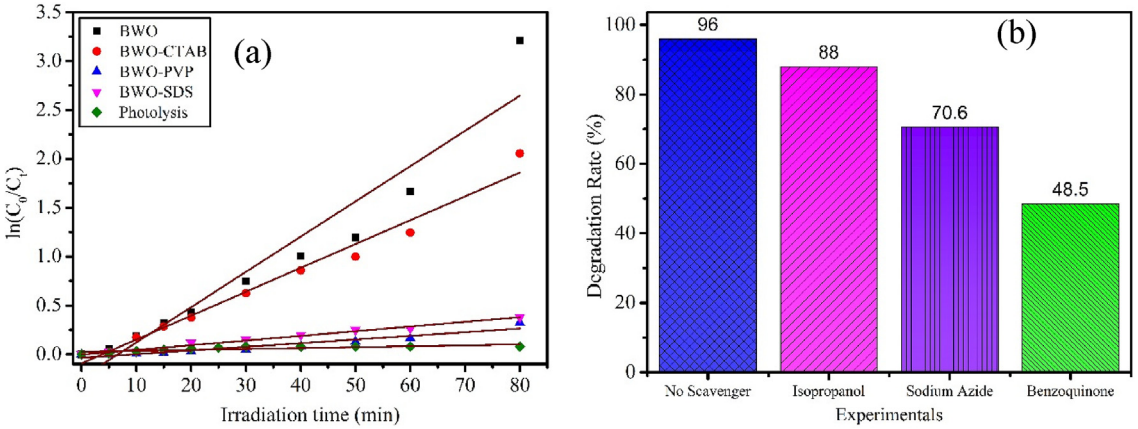

Fig. 12. (a) Reaction kinetic curve of degradation of the RhB under light irradiation (370 nm) using catalysts. (b) Histograms of degradation of the Rh 6G under photocatalysis using a scavenger.

(new morphologies) enough to achieve narrower band gap (better absorption in the visible light) without introducing localized state within the band gap, thus shifting optical absorption edge to the longer visible range improving photocatalytic activity. However, hence the band gap value to BWO-PVP and BWO-SDS sample has been reduced when compared with BWO, their photocatalytic activity was not enhanced. Here, we suggest that during synthesis process were created new localized state near VB and CB, which are responsible to high recombination of charges rate affecting the efficiency of photocatalysis, justifying the low photocatalytic activity to BWO-PVP and BWO-SDS samples.

4. Conclusions

New structures of Bi_2WO_6 were obtained, which were confirmed using XRD, SEM, Raman spectra and theoretical calculation. The investigation of their optical properties showed that because the templates react in the medium, structures with different band gap values and PL intensity are obtained, which strongly influence the photocatalytic properties. The BWO sample exhibited superior photocatalysis properties for the degradation of RhB dye, as compared with other catalysts, which was attributed to the higher crystallinity and low recombination rates of e'/h$^{\bullet}$ pairs with a decrease of intermediate levels between the VB and CB as shown in the band structure. Although we obtained a well-defined morphology of BWO-PVP (rose-like), the characterizations indicate that the high defect concentration was responsible for the high recombination of e'/h$^{\bullet}$ pairs, which was supported by PL experiments.

Acknowledgments

The authors appreciate the support of the Brazilian research financing institutions: FAPEMA (Proc. Universal-00563/15, INFRA-03965/15), CNPq (150949/2018-9) and FAPESP (grant#2013/07296-2 and grant#2013/23995-8). They also wish to thank Rorivaldo Camargo for technical and scientific contributions.

References

[1] V. Geissen, H. Mol, E. Klumpp, G. Umlauf, M. Nadal, M. van der Ploeg, S.E.A.T.M. van de Zee, C.J. Ritsema, Emerging pollutants in the environment: a challenge for water resource management, Int. Soil Water Conserv. Res. 3 (1) (2015) 57–65.
[2] M. Rani, U. Shanker, V. Jassal, Recent strategies for removal and degradation of persistent & toxic organochlorine pesticides using nanoparticles: a review, J. Environ. Manag. 190 (Supplement C) (2017) 208–222.
[3] M.S. Bootharaju, T. Pradeep, Understanding the degradation pathway of the pesticide, chlorpyrifos by noble metal nanoparticles, Langmuir 28 (5) (2012) 2671–2679.
[4] R.S. Thakur, R. Chaudhary, C. Singh, Fundamentals and applications of the photocatalytic treatment for the removal of industrial organic pollutants and effects of operational parameters: a review, J. Renew. Sustain. Energy 2 (4) (2010) 42701–42738.
[5] H. Kazuhito, I. Hiroshi, F. Akira, TiO 2 photocatalysis: a historical overview and future prospects, Jpn. J. Appl. Phys. 44 (12R) (2005) 8269.
[6] K. Mogyorósi, A. Farkas, I. Dékány, I. Ilisz, A. Dombi, TiO2-Based photocatalytic degradation of 2-chlorophenol adsorbed on hydrophobic clay, Environ. Sci. Technol. 36 (16) (2002) 3618–3624.
[7] P. Saharan, G.R. Chaudhary, S.K. Mehta, A. Umar, Removal of water contaminants by iron oxide nanomaterials, J. Nanosci. Nanotechnol. 14 (2014) 627–643.
[8] J. Liu, H. Cao, J. Xiong, Z. Cheng, Ferromagnetic hematite@graphene nanocomposites for removal of rhodamine B dye molecules from water, CrystEngComm 14 (16) (2012) 5140–5144.
[9] R. Otero, J.M. Fernández, M.A. González, I. Pavlovic, M.A. Ulibarri, Pesticides adsorption–desorption on Mg–Al mixed oxides. Kinetic modeling, competing factors and recyclability, Chem. Eng. J. 221 (2013) 214–221.
[10] S. Dong, J. Feng, M. Fan, Y. Pi, L. Hu, X. Han, M. Liu, J. Sun, J. Sun, Recent developments in heterogeneous photocatalytic water treatment using visible light-responsive photocatalysts: a review, RSC Adv. 5 (19) (2015) 14610–14630.
[11] S. Sun, W. Wang, Advanced chemical compositions and nanoarchitectures of bismuth based complex oxides for solar photocatalytic application, RSC Adv. 4 (88) (2014) 47136–47152.
[12] M.M. Khin, A.S. Nair, V.J. Babu, R. Murugan, S. Ramakrishna, A review on nanomaterials for environmental remediation, Energy Environ. Sci. 5 (8) (2012) 8075–8109.
[13] M. Maczka, J. Hanuza, W. Paraguassu, A.G. Souza, P.T.C. Freire, J. Mendes, Phonons in ferroelectric Bi2WO6: Raman and infrared spectra and lattice dynamics, Appl. Phys. Lett. 92 (11) (2008) 112911.
[14] P.L. Rocha, D.A. Batista Barbosa, J.R. de Oliveira Lima, G.M. Piedade Prazeres, C.W. de Araujo Paschoal, M.S. Li, E. Longo, A.P. Maciel, M.A.P. Almeida, Enhancement of symmetry-induced photoluminescence in bismuth tungstate microcrystals, Mater. Lett. 184 (2016) 298–300.
[15] N. Zhang, R. Ciriminna, M. Pagliaro, Y.J. Xu, Nanochemistry-derived Bi2WO6 nanostructures: towards production of sustainable chemicals and fuels induced by visible light, Chem. Soc. Rev. 43 (15) (2014) 5276–5287.
[16] Y.H. Zhang, N. Zhang, Z.R. Tang, Y.J. Xu, Identification of Bi2WO6 as a highly selective visible-light photocatalyst toward oxidation of glycerol to dihydroxyacetone in water, Chem. Sci. 4 (4) (2013) 1820–1824.
[17] M. Chen, W. Chu, Photocatalytic degradation and decomposition mechanism of fluoroquinolones norfloxacin over bismuth tungstate: experiment and mathematic model, Appl. Catal. B Environ. 168–169 (Supplement C) (2015) 175–182.
[18] Y.J. Liu, R. Cai, T. Fang, J.G. Wu, A. Wei, Low temperature synthesis of Bi2WO6 and its photocatalytic activities, Mater. Res. Bull. 66 (2015) 96–100.
[19] Y. Liu, W. Wang, Z. Fu, H. Wang, Y. Wang, J. Zhang, Nest-like structures of Sr doped Bi2WO6: synthesis and enhanced photocatalytic properties, Mater. Sci. Eng., B 176 (16) (2011) 1264–1270.
[20] Crystal. http://www.crystal.unito.it/Basis_Sets/Ptable.html, 2014.
[21] R.M. Silva, D.A. Batista Barbosa, C. de Jesus Silva Mendonça, J.R. de Oliveira Lima, F.C. Silva, E. Longo, A.P. Maciel, C.W. de Araujo Paschoal, M.A.P. Almeida, Morphological evolution and visible light-induced degradation of Rhodamine 6G by nanocrystalline bismuth tungstate prepared using a template-based approach, J. Phys. Chem. Solids 96–97 (Supplement C) (2016) 83–91.
[22] P.L. Rocha, D.A. Batista Barbosa, J.R. de Oliveira Lima, G.M. Piedade Prazeres, C.W. de Araujo Paschoal, M.S. Li, E. Longo, A.P. Maciel, M.A.P. Almeida, Enhancement of symmetry-induced photoluminescence in bismuth tungstate microcrystals 184 (Supplement C) (2016) 298–300.
[23] R. Dovesi, V.R. Saunders, C. Roetti, R. Orlando, C.M. Zicovich-Wilson, B.C.F. Pascale, K. Doll, N.M. Harrison, I.J. Bush, P. D'Arco, M. Llunel, M. Causà, Y. Noël, in: U.o. Turin (Ed.), CRYSTAL14 User's Manual, Theoretical Chemistry Group, 2014. Italy.
[24] R. Dovesi, R. Orlando, A. Erba, C.M. Zicovich-Wilson, B. Civalleri, S. Casassa, L. Maschio, M. Ferrabone, M. De La Pierre, P. D'Arco, Y. Noel, M. Causa, M. Rerat,

B. Kirtman, CRYSTAL14: a program for the ab initio investigation of crystalline solids, Int. J. Quantum Chem. 114 (19) (2014) 1287–1317.
[25] A.D. Becke, Density-functional thermochemistry .3. The role of exact exchange, J. Chem. Phys. 98 (7) (1993) 5648–5652.
[26] C. Lee, W. Yang, R.G. Parr, Development of the Colle-Salvetti correlation-energy formula into a functional of the electron density, Phys. Rev. B 37 (2) (1988) 785–789.
[27] X. Ding, K. Zhao, L. Zhang, Enhanced photocatalytic removal of sodium pentachlorophenate with self-doped Bi2WO6 under visible light by generating more superoxide ions, Environ. Sci. Technol. 48 (10) (2014) 5823–5831.
[28] J. Tauc, A. Menth, States in the gap, J. Non-Crystalline Solid 8–10 (1972) 569–585.
[29] L.W. Finger, D.E. Cox, A.P. Jephcoat, A correction for powder diffraction peak asymmetry due to axial divergence, J. Appl. Crystallogr. 27 (1994) 892–900.
[30] P.W. Stephens, Phenomenological model of anisotropic peak broadening in powder diffraction, J. Appl. Crystallogr. 32 (1999) 281–289.
[31] V.D. Nithya, R. Kalai Selvan, D. Kalpana, L. Vasylechko, C. Sanjeeviraja, Synthesis of Bi2WO6 nanoparticles and its electrochemical properties in different electrolytes for pseudocapacitor electrodes, Electrochim. Acta 109 (2013) 720–731.
[32] K. Momma, F. Izumi, VESTA 3 for three-dimensional visualization of crystal, volumetric and morphology data, J. Appl. Crystallogr. 44 (2011) 1272–1276.
[33] H.C. Gupta, Archana, V. Luthra, Lattice dynamical investigations for Raman and infrared frequencies of Bi2WO6, J. Mol. Struct. 1005 (1–3) (2011) 53–58.
[34] H. Djani, P. Hermet, P. Ghosez, First-principles characterization of the P21ab ferroelectric phase of aurivillius Bi_2WO_6 118 (25) (2014) 13514–13524.
[35] S.M.M. Zawawi, R. Yahya, A. Hassan, H. Mahmud, M.N. Daud, Structural and optical characterization of metal tungstates (MWO4; M=Ni, Ba, Bi) synthesized by a sucrose-templated method, Chem. Cent. J. 7 (2013) 1–10.
[36] M. Maczka, L. Macalik, S. Kojima, Temperature-dependent Raman scattering study of cation-deficient Aurivillius phases: Bi2WO6 and Bi2W2O9, J. Phys. Condens. Matter 23 (40) (2011) 405902.
[37] X.Y. Kong, Y.Y. Choo, S.-P. Chai, A.K. Soh, A.R. Mohamed, Oxygen vacancy induced Bi2WO6 for the realization of photocatalytic CO2 reduction over the full solar spectrum: from the UV to the NIR region, Chem. Commun. 52 (99) (2016) 14242–14245.
[38] C.M. Li, G. Chen, J.X. Sun, H.J. Dong, Y. Wang, C. Lv, Construction of Bi2WO6 homojunction via QDs self-decoration and its improved separation efficiency of charge carriers and photocatalytic ability, Appl. Catal. B Environ. 160 (2014) 383–389.
[39] V. Luca, S. Djajanti, R.F. Howe, Structural and electronic properties of sol-gel titanium oxides studied by X-ray absorption spectroscopy, J. Phys. Chem. B 102 (52) (1998) 10650–10657.
[40] J. Li, D. Chu, Energy band engineering of metal oxide for enhanced visible light absorption, in: Z. Lin, M. Ye, M. Wang (Eds.), Multifunctional Photocatalytic Materials for Energy, Woodhead Publishing, United Kingdom, 2018, p. 344.
[41] P.K. Pandey, N.S. Bhave, R.B. Kharat, Structural, optical, electrical and photovoltaic electrochemical characterization of spray deposited NiWO4 thin films, Electrochim. Acta 51 (22) (2006) 4659–4664.